

# HACT-Net: A Hierarchical Cell-to-Tissue Graph Neural Network for Histopathological Image Classification

Pushpak Pati\*<sup>1,2</sup> Guillaume Jaume\*<sup>2,3</sup> Lauren Alisha Fernandes<sup>1</sup> Antonio Foncubierta<sup>3</sup> Florinda Feroce<sup>4</sup>

Anna Maria Anniciello<sup>4</sup> Giosue Scognamiglio<sup>4</sup> Nadia Brancati<sup>5</sup> Daniel Riccio<sup>5</sup> Maurizio Do Bonito<sup>4</sup> Giuseppe De Pietro<sup>5</sup>

Gerardo Botti<sup>4</sup> Orcun Goksel<sup>1</sup> Jean-Philippe Thiran<sup>2</sup> Maria Frucchi<sup>5</sup> Maria Gabrani<sup>3</sup>

<sup>1</sup>ETH Zurich Zurich, Switzerland    <sup>2</sup>EPFL Lausanne, Switzerland    <sup>3</sup>IBM Research Zurich, Switzerland    <sup>4</sup>IRCCS-Fondazione Pascale Naples, Italy    <sup>5</sup>ICAR-CNR Naples, Italy

**Abstract**—Cancer diagnosis, prognosis, and therapeutic response prediction are heavily influenced by the relationship between the histopathological structures and the function of the tissue. Recent approaches acknowledging the structure-function relationship, have linked the structural and spatial patterns of cell organization in tissue via cell-graphs to tumor grades. Though cell organization is imperative, it is insufficient to entirely represent the histopathological structure. We propose a novel hierarchical cell-to-tissue-graph (HACT) representation to improve the structural depiction of the tissue. It consists of a low-level cell-graph, capturing cell morphology and interactions, a high-level tissue-graph, capturing morphology and spatial distribution of tissue parts, and cells-to-tissue hierarchies, encoding the relative spatial distribution of the cells with respect to the tissue distribution. Further, a hierarchical graph neural network (HACT-Net) is proposed to efficiently map the HACT representations to histopathological breast cancer subtypes. We assess the methodology on a large set of annotated tissue regions of interest from H&E stained breast carcinoma whole-slides. Upon evaluation, the proposed method outperformed recent convolutional neural network and graph neural network approaches for breast cancer multi-class subtyping. The proposed entity-based topological analysis is more inline with the pathological diagnostic procedure of the tissue. It provides more command over the tissue modelling, therefore encourages the further inclusion of pathological priors into task-specific tissue representation.

**Keywords**-Digital Pathology; Cancer Grading; Graph Neural Networks

## I. INTRODUCTION

Breast cancer is the second most common type of cancer with high mortality rate in women [1]. A majority of breast lesions are diagnosed according to a diagnostic spectrum of cancer classes that ranges from benign to invasive. The classes confer different folds of risk to become invasive. Lesions with atypia or ductal carcinoma in-situ are associated with higher risks of transitioning to invasive carcinoma compared to benign lesions [2], [3]. Thus, accurate discrimination of these classes is pivotal to determine the optimal treatment plan. However, distinguishing the classes is not always easy, *e.g.*, in [3] pathologists' concordance rates were

as low as 48% for atypia. In a clinical setting, pathologists begin the classification of a tissue biopsy by discerning the morphology and the spatial distribution of tissue parts, such as epithelium, stroma, necrosis etc. Then, they localize their analysis to specific regions of interest (RoI) on the tissue and evaluate nuclear phenotype, morphology, topology and tissue distribution among several other criteria for the classification. However, such inspections are tedious, time-consuming and prone to observer variability, thus increasing the demand for automated systems in cancer diagnosis. Digital pathology has recently motivated innovative research opportunities in machine learning and computer vision to automate cancer diagnosis [4]. The most common technique for classifying RoIs consists of extracting fixed-size patches from an RoI and classifying them using Convolutional Neural Networks (CNN); then, patch-based predictions are aggregated to label the RoI [5], [6]. Such approaches are limited to finding the apt patch size and resolution to include context information. It can be achieved by reducing the resolution at the cost of missing cell-level information, or by increasing the resolution at the cost of limiting patch size due to computational challenges. Additionally, patch-based approaches unfairly assume the same label for an RoI and its corresponding patches. Further, the pixel-based analysis by the CNNs do not comprehend the essence of biological entities and their biological context. This inhibits the integration of CNNs and prior pathological knowledge that would require selective entity-based application of CNNs.

To address the above issues, histopathological structures of tissues have been represented by cell-graphs (CG) [7], where cells and cellular interactions are presented as nodes and edges of CG respectively. Then, classical graph learning techniques or graph neural networks (GNNs) learn from CGs to map the structure-function relationship. Recently various CG representations [8]–[11] have been proposed by varying the graph building strategies or the node attributes. However, a CG exploits only the cellular morphology and topology, and discards the tissue distribution information

such as the stromal microenvironment, tumor microenvironment, lumen structure etc. that are vital for appropriate representation of histopathological structures. Additionally, a CG cannot represent the hierarchical nature of the tissue. For instance, in [10], a hierarchy is defined from the cells with learned pooling layers. However, the tissue hierarchy is inaccessible as the representation does not include high-level tissue features. In [12], the cell-level and tissue-level information are simply concatenated. Thus, the functional representation of the tissue cannot leverage the hierarchy between the levels.

We address the above shortcomings by proposing a novel Hierarchical-Cell-to-Tissue (HACT) representation of the RoIs. In HACT representation, a low-level CG captures the cellular morphology and topology; a high-level tissue-graph (TG) captures the attributes of the tissue parts and their spatial distribution; and the hierarchy between the CG and the TG captures the relative distribution of the cells with respect to the tissue distribution. Further, we propose HACT-Net, a hierarchical GNN to learn from the HACT representation and predict cancer types. Similar to the RoI diagnostic procedure by the pathologist’s, HACT-Net encodes contextual local and global structural attributes and interactions, thereby allowing for enriched structure-function relation analysis.

## II. METHODS

We propose a HACT-representation that consists of a low-level CG, a high level TG and cell-to-tissue hierarchies. This representation is processed by HACT-Net, a hierarchical GNN that employs two GNNs [13]–[18] to operate at cell and tissue-level. The learned cell *node* embeddings are combined with the corresponding tissue *node* embedding via the cell-to-tissue hierarchies. Figure 1 summarizes the proposed methodology including the pre-processing for stain normalization [19], HACT-representation building and HACT-Net.

### A. Representation

We define an undirected graph  $G := (V, E)$  as a set of  $|V|$  nodes and  $|E|$  edges. An edge between the nodes  $u$  and  $v$  is denoted by  $e_{uv}$  or  $e_{vu}$ . The graph topology is described by a symmetric adjacency matrix  $A \in \mathbb{R}^{|V| \times |V|}$ , where an entry  $A_{u,v} = 1$  if  $e_{uv} \in E$ . Each node  $v$  is presented by a feature vector  $h(v) \in \mathbb{R}^d$ . Equivalently, the node features are presented in their matrix form as  $H \in \mathbb{R}^{|V| \times d}$ . We define the neighborhood of a node  $v$  as  $\mathcal{N}(v) := \{u \in V \mid v \in V, e_{uv} \in E\}$ .

1) *Cell-graph (CG)*: In a CG, each node represents a cell and edges encode cellular interactions. We detect nuclei using the Hover-Net model [20], pre-trained on the multi-organ nuclei segmentation dataset [21]. For each detected nucleus at  $40\times$  resolution, we extract hand-crafted features

representing shape, texture and spatial location following [10]. Shape features include eccentricity, area, maximum and minimum length of axis, perimeter, solidity and orientation. Texture features include average foreground and background difference, standard deviation, skewness and mean entropy of nuclei intensity, and dissimilarity, homogeneity, energy and ASM from Gray-Level Co-occurrence Matrix. Nuclei are spatially encoded by their spatial centroids normalised by the image size. In total, each nucleus is represented by 18 features, noted as  $f_{CG}$ . These features serve as the initial node embeddings in CG.

To generate the CG topology, we assume that spatially close cells encode biological interactions and should be connected in CG, and distant cells have weak cellular interactions, so they should remain disconnected in CG. To this end, we use the k-Nearest Neighbors (kNN) algorithm to build the initial topology, and prune the kNN graph by removing edges lengthier than a threshold distance  $d_{min}$ . We use  $L2$  norm in the image space to quantify the cellular distance. Formally, for each node  $v$ , an edge  $e_{vu}$  is built if  $u \in \{w \mid \text{dist}(v, w) \leq d_k \wedge \text{dist}(v, w) < d_{min}, \forall w \in V, v \in V, d_k = k\text{-th smallest distance in } \text{dist}(v, w)\}$ . In our experiments, we set  $k = 5$  and  $d_{min} = 50$  pixels, i.e.  $12.5 \mu\text{m}$  considering the scanner resolution of  $0.25 \mu\text{m/pixel}$ . Figure 2(a) presents a sample CG elucidating the nodes and edges in the zoomed-in sub-image.

2) *Tissue-graph (TG)*: To capture the tissue distribution, we construct a TG by considering interactions among the parts of the tissue. In particular, we consider the SLIC algorithm [22] emphasizing on space proximity to over-segment tissue parts into non-overlapping homogeneous super-pixels. Subsequently, to create super-pixels capturing meaningful tissue information, we hierarchically merge adjacent similar super-pixels. The similarity is measured by texture attributes, i.e., contrast, dissimilarity, homogeneity, energy, entropy and ASM from Gray-Level Co-occurrence Matrix, and channel-wise color attributes, i.e., 8-bin color histogram, mean, standard deviation, median, energy and skewness. Initial over-segmentation is performed at  $10\times$  magnification to detect more homogeneous super-pixels and to achieve computational efficiency in super-pixel detection. Finally, color and texture features are extracted for the merged super-pixels at  $40\times$  magnification to capture informative local attributes. A supervised random-forest feature selection is employed and 24 dominant features are selected that classify the super-pixels into epithelium, stroma, necrosis and background tissue parts. Additionally, spatial centroids of super-pixels normalised by the image size are included to construct 26-dimensional representations for the super-pixels.

To generate the TG topology, we assume that adjacent tissue parts biologically interact and should be connected. To this end, we construct a region adjacency graph (RAG) [23] using the spatial centroids of the super-pixels. The

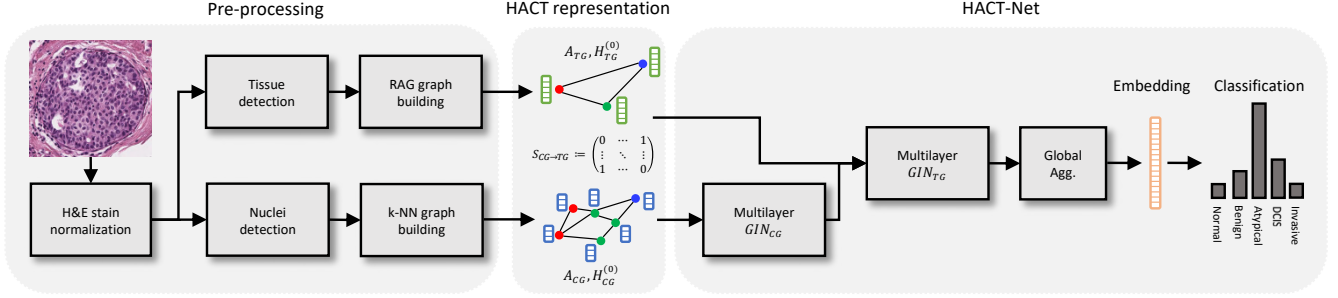


Figure 1: Block diagram of the proposed methodology including pre-processing module, HACT representation of a RoI and HACT-Net classifying the RoI.

super-pixel attributes define the initial node features, noted as  $f_{TG}$  and the RAG edges define the TG edges. Figure 2(b) presents a sample TG. The large node at the center represents the centroid of the surrounding stroma that is connected to the parts of epithelium and background. Thus, TG encodes information from the tumor and the stroma microenvironment.

### 3) Hierarchical-Cell-to-Tissue (HACT) representation:

To jointly represent the low-level CG and high-level TG, we introduce HACT defined as  $G_{HACT} := \{G_{CG}, G_{TG}, S_{CG \rightarrow TG}\}$ .  $G_{CG} = (V_{CG}, E_{CG})$  and  $G_{TG} = (V_{TG}, E_{TG})$  are CG and TG respectively. We introduce an assignment matrix  $S_{CG \rightarrow TG} \in \mathbb{R}^{|V_{CG}| \times |V_{TG}|}$  that describes a pooling operation to topologically map CG to TG.  $S_{CG \rightarrow TG}$  is built using the spatial information of nuclei and super-pixels, *i.e.*,  $S_{CG \rightarrow TG}(i, j) = 1$  if the nucleus represented by node  $i$  in CG spatially belongs to the super-pixel represented by node  $j$  in TG. Note that  $|V_{CG}| \gg |V_{TG}|$ . An overview of HACT in Figure 2(c) displays the multi-level graphs and the hierarchies.

### B. HACT Graph Neural Networks (HACT-Net)

HACT-Net processes a multi-scale representation of the tissue. Given  $G_{HACT}$ , we learn a graph-level embedding  $h_{HACT} \in \mathbb{R}^{d_{HACT}}$  that is input to a classification neural network to predict the classes. We use the Graph Isomorphism Network (GIN) [17], an instance of message passing neural network [18] with a provably strong expressive power to learn fixed-size discriminative graph embeddings.

First, we apply  $T_{CG}$  GIN layers on  $G_{CG}$  to build contextualised cell-node embeddings. For a node  $u$ , we iteratively update the node embedding as:

$$h_{CG}^{(t+1)}(u) = \text{MLP}\left(h_{CG}^{(t)}(u) + \sum_{w \in \mathcal{N}_{CG}(u)} h_{CG}^{(t)}(w)\right) \quad (1)$$

where,  $t = 0, \dots, T_{CG}$ ,  $\mathcal{N}_{CG}(u)$  denotes the set of neighborhood cell-nodes of  $u$ , and MLP is a multi-layer

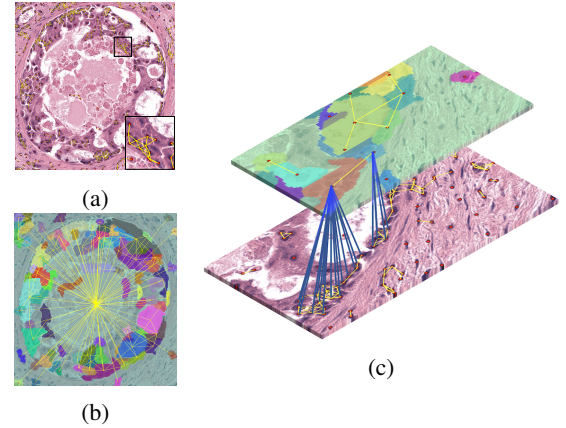


Figure 2: Visualizing (a) CG, (b) TG, and (c) HACT representations. Nodes are presented in red and edges in yellow. Cell-to-tissue hierarchies are shown in blue in HACT. Note that all hierarchies in HACT are not shown for visual clarity.

perceptron. At  $t = 0$ , the initial node embedding is, *i.e.*,  $h_{CG}^{(0)}(u) = f_{CG}(u)$ . After  $T_{CG}$  GIN layers, the node embeddings  $\{h_{CG}^{(T_{CG})}(u) \mid u \in V_{CG}\}$  are used as additional tissue-node features, *i.e.*,

$$h_{TG}^{(0)}(v) = \text{Concat}\left(f_{TG}(v), \sum_{u \in \mathcal{S}(v)} h_{CG}^{(T_{CG})}(u)\right) \quad (2)$$

where,  $\mathcal{S}(v) := \{u \in V_{CG} \mid S_{CG \rightarrow TG}(u, v) = 1\}$  denotes the set of nodes in  $G_{CG}$  mapping to a node  $v \in V_{TG}$  in  $G_{TG}$ . Analogous to Equation (1), we apply the second graph neural network based on GIN layers to  $G_{TG}$  to compute the tissue-node embeddings  $\{h_{TG}^{(t)}(v) \mid v \in V_{TG}\}$ . At  $t = T_{TG}$ , each tissue-node embeddings encode the cellular and tissue information up to  $T_{TG}$ -hops from  $v$ .

Finally, the graph level representation  $h_{HACT}$  is built by concatenating the aggregated node embeddings of  $G_{TG}$  from all layers [17], *i.e.*,

$$h_{\text{HACT}} = \text{Concat}\left(\left\{\sum_{v \in G_{\text{TG}}} h_{\text{TG}}^{(t)}(v) \mid t = 0, \dots, T_{\text{TG}}\right\}\right) \quad (3)$$

The graph-level representations are then processed by an MLP classifier to predict the cancer subtype.

### III. EXPERIMENTAL RESULTS

#### A. Dataset

We introduce a new dataset for BReAst Carcinoma Subtyping (**BRACS**)<sup>1</sup>. BRACS consists of 2080 RoIs acquired from 106 H&E stained breast carcinoma whole-slide-images (WSI). The WSIs are scanned with Aperio AT2 scanner at  $0.25 \mu\text{m}/\text{pixel}$  for  $40\times$  resolution. RoIs are selected and annotated as: Normal, Benign (includes Benign and Usual ductal hyperplasia), Atypical (includes Flat epithelial atypia and Atypical ductal hyperplasia), Ductal carcinoma in situ and Invasive, by the consensus of three pathologists using QuPath [24]. BRACS is more than four times the size of the popular BACH dataset [6] and consists of challenging typical and atypical hyperplasia subtypes. Unlike BACH, BRACS exhibits large variability in the RoI dimensions as shown in Table I. The RoIs represent a more realistic scenario by including single and multiple glandular regions, and comprising of prominent diagnostic challenges such as stain variance, tissue preparation artifacts and tissue marking artifacts. Unlike recent graph-based approaches on histopathology data [10]–[12] that conduct data splitting at image level, we perform train, validation and test RoI splits at the WSI-level, such that two images from the same slide does not belong to different splits. RoIs from the same WSI can be morphologically and structurally correlated, even if they are non-overlapping. Thus, image-level splitting leads to over-estimated results on the evaluation set, and networks trained in such manner lack generalizability to unseen data. We consider four sets of train, validation and test splits, generated at random at the WSI-level, to evaluate our methodology.

#### B. Implementation

All our experiments are conducted using PyTorch [26] and the DGL library [27]. We benchmark our proposed method, HACT-Net, against several GNN- and CNN-based approaches. We compare HACT-Net with standalone CG-GNN and TG-GNN to assess the impact of multi-level information processing. We compare HACT-Net with Concat-GNN that concatenates the CG and TG graph embeddings, *i.e.*,  $h_{\text{Concat}} = \text{Concat}(h_{\text{CG}}, h_{\text{TG}})$ , to evaluate the benefit of hierarchical-graph learning. Note that Concat-GNN is analogous to the recently proposed Pathomic Fusion by [12]. For the CNN approaches, we implement single scale CNNs

<sup>1</sup>currently pending approval for releasing the dataset to the research community

[25] at three magnifications. Further, we compare with two multi-scale CNNs utilizing late fusion with single stream + LSTM architecture [25]. The multi-scale CNNs use multi-scale patch information from ( $10\times + 20\times$ ) and ( $10\times + 20\times + 40\times$ ). Considering tumor heterogeneity, CNN approaches are limited to  $10\times$  magnification so that only one cancer type is included in an RoI.

The CG-GNN and TG-GNN have four GIN layers with a hidden dimension of 32 in standalone, Concat-GNN and HACT-Net. Each GIN layer uses a 2-layer MLP with ReLU activation. The classifier is composed of a 2-layer MLP with 64 hidden neurons and five output neurons, *i.e.*, the number of classes. The model is trained to minimize the cross-entropy loss between the output logits and the ground truth labels. We set the batch size to 16, the initial learning rate to  $10^{-3}$  and use the Adam [28] optimizer with a weight decay of  $5 \cdot 10^{-4}$ . For the single-scale and multi-scale CNNs, we extract patches of size  $128 \times 128$  at  $10\times$ ,  $20\times$  and  $40\times$ . Pre-trained ResNet-50 on ImageNet is finetuned to obtain patch-level feature representations after experimenting with different ResNet, VGG-Net and DenseNet architectures. All the CNNs use [5] to derive RoI-level feature representation via aggregate-penultimate technique, and employ a 2-layer MLP with 64 hidden neurons and five output neurons for RoI classification. Considering the per-class data imbalance, weighted F1-score is used to quantify the classification performance. Model with the best weighted F1-score on the validation set is selected as the final model in each approach.

#### C. Discussion

Figure 3 demonstrates CG and TG representation of sample *rois* from BRACS dataset. Visual inspection signifies that the constructed CGs aptly encompass the cellular distribution and cellular interactions. Similarly, the TGs aptly encode the tissue microenvironment by including the topological distribution of the tissue components. The TGs include lumen in Benign, apical snouts in Atypical, necrosis in DCIS and tumor-associated stroma in DCIS and Invasive that are not accessible to the CGs.

Table II presents the weighted F1-score on four test folds and their aggregate statistics for the networks. The standalone CNNs perform better while operating at lower magnification as they capture larger context. The multi-scale CNNs perform better by including local and global context information from multiple magnifications. The CG-GNN and TG-GNN results signify that topological entity-based paradigm is superior to pixel-based CNNs. Further, they indicate that tissue distribution information is inferior to nuclei distribution information for breast cancer subtyping. Our CG-GNN baseline outperforms CGCNet [10] justifying the use of expressive backbone GNNs like GIN [17]. We also hypothesize that simply concatenating the updated node representation at *each* layer as shown in Equation 3 brings a performance boost without additional parameters. Concat-

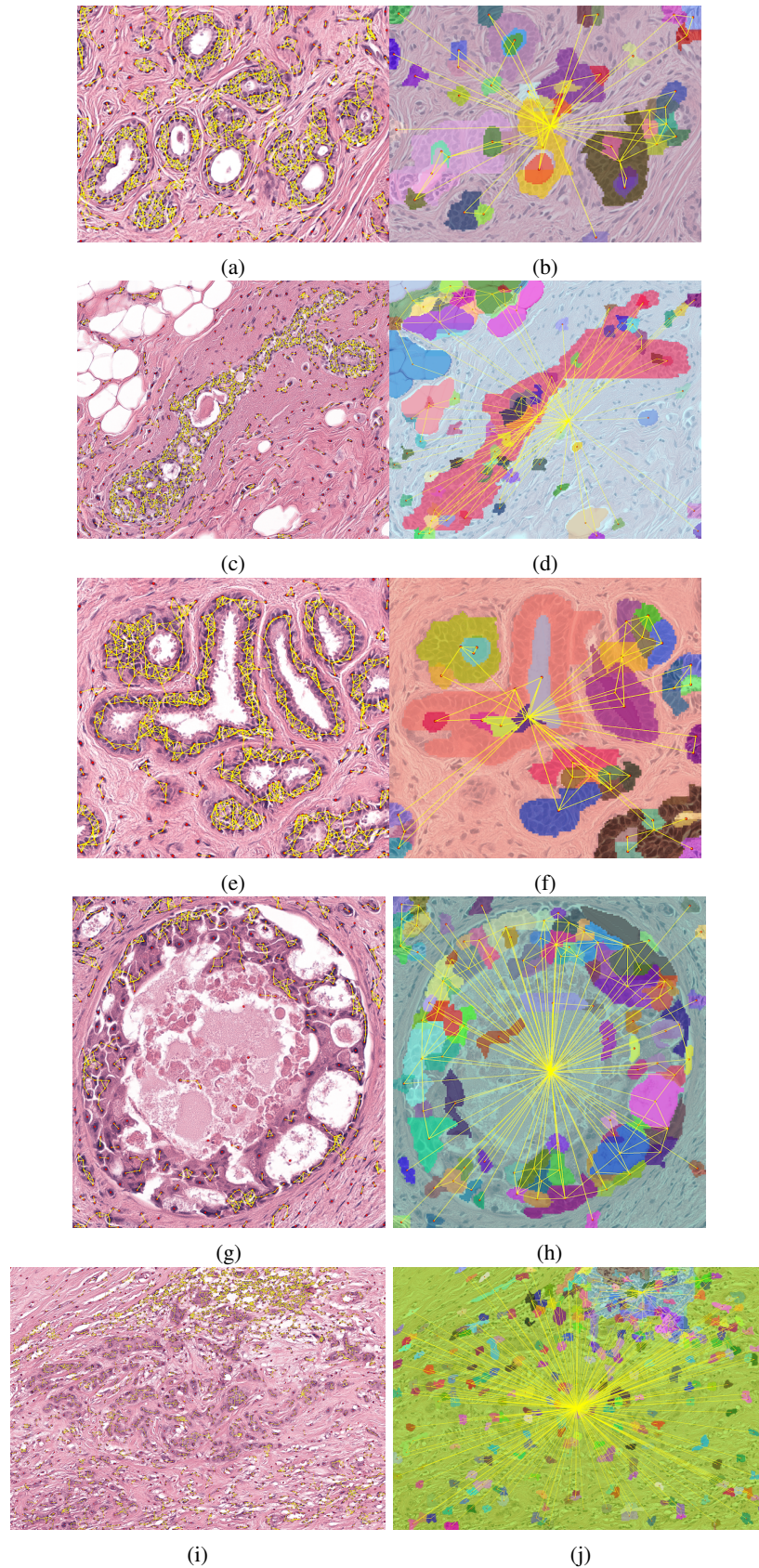


Figure 3: Cell-graph (left) and tissue-graph (right) examples for four cancer subtypes. (a-b) Normal, (c-d) Benign, (e-f) Atypical, (g-h) DCIS, and (i-j) Invasive. Large central nodes in the tissue-graphs depict the centroids of the surrounding stroma tissues.

Table I: BReAst Carcinoma Subtyping (BRACS) dataset statistics.

	Normal	Benign	Atypical	DCIS	Invasive	Total
# RoI	305	462	387	503	423	2080
Avg. # pixels in a RoI	2.1M	5.8M	1.4M	4.4M	9.6M	4.9M
Avg. # nodes in a Cell-graph	841	2125	584	1740	4176	1974
Avg. # nodes in a Tissue-graph	80	222	70	205	487	223

Fold~Tr/V/Te	Normal	Benign	Atypical	DCIS	Invasive	Total
Fold 1	198/60/47	318/78/66	244/75/68	359/76/68	286/70/67	1405/359/316
Fold 2	202/47/56	304/66/92	245/68/74	355/68/80	283/67/73	1389/316/375
Fold 3	200/56/49	278/92/92	234/74/79	346/80/77	282/73/68	1340/375/365
Fold 4	196/49/60	292/92/78	233/79/75	350/77/76	285/68/70	1356/365/359

Table II: Weighted F1-scores across four test folds. Mean and standard deviation of fold-wise and class-wise weighted F1-scores. Results expressed in %.

Model/Fold#	1	2	3	4	$\mu \pm \sigma$	Normal	Benign	Atypical	DCIS	Invasive
CNN (10 $\times$ ) [5], [25]	49.85	46.86	51.19	54.04	50.49 $\pm 2.58$	47.50 $\pm 2.50$	46.00 $\pm 7.45$	39.25 $\pm 3.63$	51.25 $\pm 2.05$	69.75 $\pm 4.21$
CNN (20 $\times$ ) [5], [25]	52.49	51.88	44.38	56.37	51.28 $\pm 4.34$	52.25 $\pm 1.64$	47.25 $\pm 6.80$	44.50 $\pm 4.56$	48.25 $\pm 3.56$	62.25 $\pm 4.44$
CNN (40 $\times$ ) [5], [25]	40.64	47.30	38.08	48.95	43.74 $\pm 4.51$	46.00 $\pm 7.71$	35.50 $\pm 8.96$	46.75 $\pm 5.02$	38.00 $\pm 4.30$	56.00 $\pm 7.12$
Multi-scale CNN (10 $\times$ +20 $\times$ ) [5], [25]	56.17	54.41	53.94	55.66	55.04 $\pm 0.90$	57.25 $\pm 3.90$	51.75 $\pm 8.78$	42.25 $\pm 8.73$	54.50 $\pm 2.06$	72.25 $\pm 1.92$
Multi-scale CNN (10 $\times$ +20 $\times$ +40 $\times$ ) [5], [25]	58.80	54.64	55.53	53.90	55.72 $\pm 1.87$	55.75 $\pm 1.78$	52.25 $\pm 6.38$	46.75 $\pm 2.28$	50.75 $\pm 2.38$	71.75 $\pm 3.34$
CGCNet [10]	51.54	58.97	56.70	50.44	54.41 $\pm 3.53$	53.00 $\pm 2.55$	52.25 $\pm 4.96$	42.00 $\pm 8.15$	57.00 $\pm 5.52$	68.25 $\pm 2.58$
TG-GNN	54.47	55.13	67.84	49.85	56.82 $\pm 6.67$	56.78 $\pm 1.89$	54.76 $\pm 6.62$	48.52 $\pm 8.76$	56.53 $\pm 12.78$	69.52 $\pm 11.00$
CG-GNN	61.35	53.81	62.00	55.38	58.13 $\pm 3.59$	62.66 $\pm 5.32$	<b>64.57</b> $\pm 9.05$	36.18 $\pm 6.85$	59.98 $\pm 1.43$	68.12 $\pm 2.52$
Concat-GNN	54.66	54.49	64.59	<b>63.95</b>	59.42 $\pm 4.85$	57.00 $\pm 4.06$	60.31 $\pm 8.36$	49.62 $\pm 4.71$	60.65 $\pm 4.94$	68.94 $\pm 12.47$
HACT-Net	<b>62.17</b>	<b>59.06</b>	<b>69.41</b>	60.92	<b>62.89</b> $\pm 3.92$	<b>65.15</b> $\pm 3.64$	58.40 $\pm 10.59$	<b>55.45</b> $\pm 5.19$	<b>63.15</b> $\pm 4.08$	<b>73.78</b> $\pm 7.35$

GNN outperforms TG-GNN and CG-GNN indicating that CG and TG provide valuable complementary information. Further, HACT-Net outperforms Concat-GNN confirming that the *relationship* between the low and high-level information must be modeled at the local node-level rather than at the graph-level for better structure-function mapping.

The class-wise performance analysis in Table II shows that invasive category is the best detected. It translates to the topologically recognizable patterns with scattered nodes and edges in CG and TG. Atypical cases are the hardest to model, partially as they have a high intra-class variability and high inter-class ambiguity with benign and DCIS. Large drops in performance in the CGCNet and CG-GNN for the atypical category convey that the standalone cell information is not discriminative enough to identify these patterns. Tissue information such as apical snouts in FEA, necrosis in DCIS, stroma microenvironment in Benign etc. bolster the discriminability of atypical RoIs. Thus, all the networks including TG perform better than CG-GNN for the atypical

category. The CG-GNN and TG-GNN performances for the Normal, Benign and DCIS indicate that nuclei information is more informative to identify these categories. HACT-Net utilizes both nuclei and tissue distribution properties, thus performing superior to CG-GNN and TG-GNN for almost all subtypes. Unlike CG-GNN, HACT-Net utilizes stromal microenvironment around the tumor regions which is a pivotal factor in breast cancer development [29]. The class-wise comparison between HACT-Net and Concat-GNN establish the positive impact of hierarchical learning. The gain in class-wise performances of HACT-Net substantiates that the network does not get biased towards one particular class.

Moreover, the paradigm shift from pixel-based analysis to entity-based analysis can potentially yield interpretability of the deep learning techniques in digital pathology. For instance, [10] analyzes the cluster assignment of each node in CG representation to conclude that the clustering operation groups cells according to their appearance and

tissue belongingness. [30] introduced a novel post-hoc interpretability module on top of the learned CG-GNN to identify decisive sets of cells and cellular interactions. However, both approaches are limited to CG analysis. Since HACT-representation captures entity-based multi-level hierarchical tissue attributes similar to pathological diagnostic procedure, the interpretability of HACT-representation can identify crucial entities, such as nuclei, tissue parts and cell-to-tissue interactions, to imitate the pathologist’s assessment.

#### IV. CONCLUSION

In this work, we have proposed a novel hierarchical tissue representation in combination with a hierarchical GNN to map the histopathological structure to function relationship. We have extensively evaluated the proposed methodology and compared with the state-of-the-art CNNs and GNNs for breast cancer subtyping. The enriched multi-level topological representation and hierarchical learning scheme strengthens the proposed methodology to result in superior classification performance. The HACT-representation can seamlessly scale to any sized RoI to incorporate local and global context for improved stratification. The entity-based graphical representation yields better control for tissue encoding, and favors the inclusion of pathological context into the modeling. The success of our methodology inspires to explore approaches to further include pathological priors. Further, the hierarchical modeling paves way for recent interpretability techniques in digital pathology to go beyond cell-graphs to interpret the hierarchical nature of the tissue.

#### REFERENCES

- [1] R. L. Siegel, K. D. Miller, and A. Jemal, “Cancer statistics, 2016,” *CA: A Cancer Journal for Clinicians*, vol. 66, no. 1, pp. 7–30, 2016.
- [2] D. J. Myers and A. L. Walls, “Atypical breast hyperplasia,” in *StatPearls [Internet]*. StatPearls Publishing, 2019.
- [3] J. G. Elmore, G. M. Longton, P. A. Carney, B. M. Geller, T. Onega, A. N. A. Tosteson, H. D. Nelson, M. S. Pepe, K. H. Allison, S. J. Schnitt, F. P. OMalley, and D. L. Weaver, “Diagnostic Concordance Among Pathologists Interpreting Breast Biopsy Specimens,” *JAMA*, vol. 313, no. 11, pp. 1122–1132, 2015.
- [4] G. Litjens, T. Kooi, B. E. Bejnordi, A. A. A. Setio, F. Ciompi, M. Ghafoorian, J. A. Van Der Laak, B. Van Ginneken, and C. I. Sánchez, “A survey on deep learning in medical image analysis,” *Medical image analysis*, vol. 42, pp. 60–88, 2017.
- [5] C. Mercan, S. Aksoy, E. Mercan, L. G. Shapiro, D. L. Weaver, and J. G. Elmore, “From patch-level to roi-level deep feature representations for breast histopathology classification,” in *SPIE Medical Imaging 2019: Digital Pathology*, vol. 10956, 2019, p. 109560H.
- [6] G. Aresta, T. Araújo, S. Kwok, S. S. Chennamsetty, M. Safwan, V. Alex, B. Marami, M. Prastawa, M. Chan, M. Donovan *et al.*, “Bach: Grand challenge on breast cancer histology images,” *Medical image analysis*, vol. 56, pp. 122–139, 2019.
- [7] C. Gunduz, B. Yener, and S. H. Gultekin, “The cell graphs of cancer,” *Bioinformatics*, vol. 20, no. suppl\_1, pp. i145–i151, 2004.
- [8] H. Sharma, N. Zerbe, D. Heim, S. Wienert, S. Lohmann, O. Hellwich, and P. Hufnagl, “Cell nuclei attributed relational graphs for efficient representation and classification of gastric cancer in digital histopathology,” in *SPIE Medical Imaging 2016: Digital Pathology*, vol. 9791, 2016, p. 97910X.
- [9] S. Gadiya, D. Anand, and A. Sethi, “Histograms: Graphs in histopathology,” *arXiv preprint arXiv:1908.05020*, 2019.
- [10] Y. Zhou, S. Graham, N. Alemi Koohbanani, M. Shaban, P.-A. Heng, and N. Rajpoot, “CGC-net: Cell graph convolutional network for grading of colorectal cancer histology images,” in *Proceedings of the IEEE International Conference on Computer Vision Workshops*, 2019.
- [11] J. Wang, R. J. Chen, M. Y. Lu, A. Baras, and F. Mahmood, “Weakly supervised prostate tma classification via graph convolutional networks,” *arXiv preprint arXiv:1910.13328*, 2019.
- [12] R. J. Chen, M. Y. Lu, J. Wang, D. F. Williamson, S. J. Rodig, N. I. Lindeman, and F. Mahmood, “Pathomic fusion: An integrated framework for fusing histopathology and genomic features for cancer diagnosis and prognosis,” *arXiv preprint arXiv:1912.08937*, 2019.
- [13] M. Defferrard, X. Bresson, and P. Vandergheynst, “Convolutional neural networks on graphs with fast localized spectral filtering,” in *Advances in neural information processing systems*, 2016, pp. 3844–3852.
- [14] W. Hamilton, Z. Ying, and J. Leskovec, “Inductive representation learning on large graphs,” in *Advances in neural information processing systems*, 2017, pp. 1024–1034.
- [15] T. N. Kipf and M. Welling, “Semi-supervised classification with graph convolutional networks,” in *International Conference on Learning Representations, ICLR*, 2017.
- [16] P. Velickovic, G. Cucurull, A. Casanova, A. Romero, P. Liò, and Y. Bengio, “Graph attention networks,” in *International Conference on Learning Representations, ICLR*, 2018.
- [17] K. Xu, W. Hu, J. Leskovec, and S. Jegelka, “How powerful are graph neural networks?” in *International Conference on Learning Representations, ICLR*, 2019.
- [18] J. Gilmer, S. S. Schoenholz, P. F. Riley, O. Vinyals, and G. E. Dahl, “Neural message passing for quantum chemistry,” in *International Conference on Machine Learning, ICML*, vol. 70, 2017, pp. 1263–1272.
- [19] M. Macenko, M. Niethammer, J. S. Marron, D. Borland, J. T. Woosley, X. Guan, C. Schmitt, and N. E. Thomas, “A method for normalizing histology slides for quantitative analysis,” in *2009 IEEE International Symposium on Biomedical Imaging: From Nano to Macro*, 2009, pp. 1107–1110.

- [20] S. Graham, Q. D. Vu, S. E. A. Raza, A. Azam, Y. W. Tsang, J. T. Kwak, and N. Rajpoot, "Hover-net: Simultaneous segmentation and classification of nuclei in multi-tissue histology images," *Medical Image Analysis*, vol. 58, p. 101563, 2019.
- [21] N. Kumar, R. Verma, S. Sharma, S. Bhargava, A. Vahadane, and A. Sethi, "A dataset and a technique for generalized nuclear segmentation for computational pathology," *IEEE transactions on medical imaging*, vol. 36, no. 7, pp. 1550–1560, 2017.
- [22] R. Achanta, A. Shaji, K. Smith, A. Lucchi, P. Fua, and S. Süsstrunk, "Slic superpixels compared to state-of-the-art superpixel methods," *IEEE transactions on pattern analysis and machine intelligence*, vol. 34, no. 11, pp. 2274–2282, 2012.
- [23] F. K. Potjer, "Region adjacency graphs and connected morphological operators," in *Mathematical Morphology and its Applications to Image and Signal Processing*, ser. Computational Imaging and Vision, vol. 5, 1996, pp. 111–118.
- [24] P. Bankhead, M. B. Loughrey, J. A. Fernández, Y. Dombrowski, D. G. McArt, P. D. Dunne, S. McQuaid, R. T. Gray, L. J. Murray, H. G. Coleman *et al.*, "Qupath: Open source software for digital pathology image analysis," *Scientific reports*, vol. 7, no. 1, pp. 1–7, 2017.
- [25] K. Sirinukunwattana, N. Alham, C. Verrill, and J. Rittscher, "Improving whole slide segmentation through visual context - a systematic study," in *Medical Image Computing and Computer Assisted Intervention, (MICCAI)*, vol. 11071, 2018.
- [26] A. Paszke, S. Gross, F. Massa, A. Lerer, J. Bradbury, G. Chanan, T. Killeen, Z. Lin, N. Gimelshein, L. Antiga *et al.*, "Pytorch: An imperative style, high-performance deep learning library," in *Advances in Neural Information Processing Systems*, 2019, pp. 8024–8035.
- [27] M. Wang, L. Yu, D. Zheng, Q. Gan, Y. Gai, Z. Ye, M. Li, J. Zhou, Q. Huang, C. Ma, Z. Huang, Q. Guo, H. Zhang, H. Lin, J. Zhao, J. Li, A. J. Smola, and Z. Zhang, "Deep graph library: Towards efficient and scalable deep learning on graphs," *CoRR*, vol. abs/1909.01315, 2019.
- [28] D. P. Kingma and J. Ba, "Adam: A method for stochastic optimization," in *International Conference on Learning Representations, ICLR*, Y. Bengio and Y. LeCun, Eds., 2015.
- [29] B. Bejnordi, M. Mullooly, R. Pfeiffer, S. Fan, P. Vacek, D. Weaver, S. Herschorn, L. Brinton, B. van Ginneken, N. Karssemeijer, A. Beck, G. Gierach, J. van der Laak, and M. Sherman, "Using deep convolutional neural networks to identify and classify tumor-associated stroma in diagnostic breast biopsies," in *Modern Pathology*, vol. 31, no. 10, 2018, pp. 1502–1512.
- [30] G. Jaume, P. Pati, F. Feroce, A. Anniciello, G. Scognamiglio, A. Foncubierta-Rodriguez, O. Goksel, J. Thiran, and M. Gabrani, "Towards explainable graph representations in digital pathology," in *International Conference on Machine Learning, Workshop on Computational Biology*, 2020.